LANGMUIR

pubs.acs.org/Langmuir Article

Universal Langmuir and Fractal Analysis of High-Resolution Adsorption Isotherms of Argon and Nitrogen on Macroporous Silica

Trevor C. Brown,* Ali Bagheri, and Christopher M. Fellows

Cite This: *Langmuir* 2023, 39, 1914−1926 Read Online

ACCESS | Metrics & More | Article Recommendations | Supporting Information

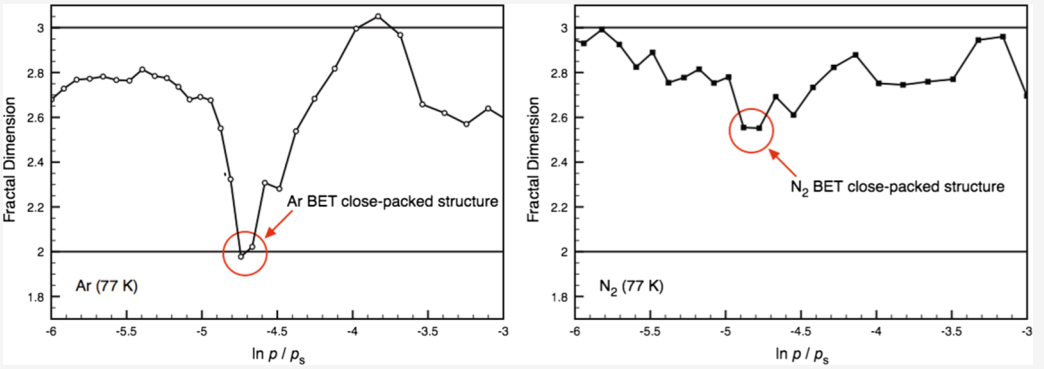

ABSTRACT: High-resolution isotherms of argon and nitrogen adsorption on macroporous silica have been simulated with universal Langmuir and fractal models. A four-parameter, fractal universal Langmuir equation is a good fit to the data at low pressures. Standard Gibbs energy changes calculated from equilibrium adsorption coefficients show a series of broad peaks that indicate adsorbate structural transformations as a function of pressure and coverage. The Freundlich equation or mean fractal model is also a good fit to isotherms at low pressures. Pressure-varying fractals are accurate fits to the data. Fractal exponents provide information on adsorbate coverage and surface access. Broad peaks in pressure-varying exponents are indicators of adsorbate structure. From adsorptive gas amounts, mean and pressure-varying fractal exponents provide details of adsorbate fractal dimensions and surface roughness. Both Ar and N_2 adsorption cause increases in mean surface roughness when compared with pure silica. Surface roughness fluctuations from pressure-dependent adsorptive gas fractal dimensions are associated with adsorbate structure. At one trough, the surface is smooth and is linked to close-packed Ar or N_2. For Ar adsorption at 87 K, this structure is a complete monolayer (1.00(4)), while for Ar (77 K), 1.15(4) layers and for N_2 (87 K), 2.02(10) layers. The universal Langmuir specific area of the silica is 10.1(4) $m^2\ g^{-1}$. Pressure- and coverage-dependent adsorbate structures range from filling defects and holes on the surface to cluster formation to adsorbed Ar or N_2 evenly distributed or packed across the surface. The Ar (87 K) isotherm is most sensitive to adsorbate structural transformations.

INTRODUCTION

A large range of isothermal adsorption models have been developed and reported to simulate experimental data sets to explore adsorbent and adsorbate properties and to optimize adsorption systems.[1,2] Most reported models simulate the equilibrium adsorption capacity or surface excess of the adsorbent, $q_e(p)$ for specific adsorption types[3] and over narrow pressure ranges.

A universal Langmuir (uL) model to describe the pressure-evolution of adsorption capacity, $q_e(p)$, for all isothermal adsorption types has recently been proposed.[4,5] This model is based on the classical, two-parameter Langmuir isotherm equation.[6] The classical equation is only applicable for homogeneous surfaces and does not account for adsorbate/adsorbate interactions. That is, the two Langmuir constants, maximum adsorption capacity, and equilibrium adsorption coefficient cannot be uniquely selected to fit most isothermal adsorption experimental data sets. The universal Langmuir equation is written with both Langmuir parameters varied at each pressure to exactly simulate the measured adsorption capacity:

$$q_e(p) = \frac{Q_{uL}(p)\, K_{uL}(p)\, p/p_s}{1 + K_{uL}(p)\, p/p_s} \quad (1)$$

Here, p/p_s are measured relative pressures and p_s is the saturated vapor pressure of the adsorptive gas. Maximum adsorption

Received: October 27, 2022
Revised: January 3, 2023
Published: January 23, 2023

https://doi.org/10.1021/acs.langmuir.2c02932
Langmuir 2023, 39, 1914−1926

capacities, $Q_{uL}(p)$, are the sum of $q_e(p)$ and the amounts of adsorptive gas, $q_{g,uL}(p)$, within the adsorption space that is in equilibrium with the absorbent:[3,7]

$$Q_{uL}(p) = q_e(p) + q_{g,uL}(p) \tag{2}$$

Equilibrium adsorption capacities, $K_{uL}(p)$, are also a function of $q_e(p)$ and $q_{g,uL}(p)$:

$$K_{uL}(p) = \frac{q_e(p)}{q_{g,uL}(p)\, p/p_s} \tag{3}$$

Both $Q_{uL}(p)$ and $K_{uL}(p)$ are calculated from measured adsorption capacities and pressures using flexible least-squares methodology.[4,5,8]

The universal Langmuir specific area of the adsorbent is the product of $Q_{uL}(p)$ and the apparent atomic or molecular cross-sectional areas of the adsorbate. With increasing collision frequency, adsorbate packing density increases and adsorbate binding strength decreases due to increasing adsorbate–adsorbate interactions[9] and the sequential filling of surface sites.[7,10] Adsorbate structural transformations with increasing pressure include the formation of ordered monolayer structures[5] and clusters[11−13] and due to adsorption-induced deformation of the adsorbent.[14,15] Shimizu and Matubayasi[16] use statistical thermodynamic fluctuation theory to identify a Point M in an isotherm, corresponding to the pressure where Brunauer–Emmett–Teller (BET) monolayer capacity is apparent. However, care must be taken when interpreting adsorption properties from experimental data that the isotherms are reproducible.[17]

Adsorption types and properties can be interpreted by exploring fractal-like trends in measured $q_e(p)$ values and in calculated uL parameters. The Frenkel–Halsey–Hill (FHH) equation for multilayer adsorption has been generalized to fractal surfaces:[18−20]

$$q_e(p) = Q^{\circ}_{FHH}\left[\ln\left(\frac{p_s}{p}\right)\right]^{\gamma_{FHH}} \tag{4}$$

Here, Q°_{FHH} is the apparent maximum adsorption capacity at p_s/e. The exponent, γ_{FHH}, is determined from the slope of a plot of $\ln q_e(p)$ against $\ln [\ln (p/p_s)]$ and is related to the surface fractal dimensions (D_e) of the adsorbent by $\gamma_{FHH} = 3 - D_e$.[20] Values of D_e are dimensionless numbers between 2 and 3 and are measures of surface geometric heterogeneity or surface roughness. For perfect smooth surfaces, $D_e = 2$, and for maximum roughness and disorder, $D_e = 3$.

Another fractal scaling relationship with a power functional form,[21] is the two-parameter Freundlich (F) isotherm equation.[22,23] It is widely used to describe nonideal, multilayer adsorption although less commonly used than eq 4 to calculate surface fractal dimensions.

$$q_e(p) = q^{\circ}_{e,F}\left(\frac{p}{p_s}\right)^{\gamma_F} \tag{5}$$

The parameter, $q^{\circ}_{e,F}$, is a Freundlich normalization constant equal to the extrapolated adsorption capacity at p_s, and the exponent, γ_F, is a constant. Fitted values of γ_F at submonolayer pressures have been used to determine surface fractal dimensions,[24−27] the energy distributions of adsorption sites,[28] and adsorbate affinity.[23] In this study, properties from these surface fractal exponents calculated from measured adsorption capacities, $q_e(p)$, maximum adsorption capacities, $Q_{uL}(p)$, and equilibrium adsorption capacities, $K_{uL}(p)$ are explored. Such analyses have not been previously reported.

In this study, flexible least-squares methodology[8] is used to calculate the universal Langmuir parameters, $Q_{uL}(p)$ and $K_{uL}(p)$, in eq 1.[4,5] The pressure-varying fractals for measured adsorption capacity amounts and universal Langmuir parameters are calculated using power functional forms of the Freundlich equation, e.g., eq 5. Parameters are determined across the full pressure range for Ar adsorption on the macroporous silica, LiChrospher Si-1000 (LiC) at 77 and 87 K and for nitrogen adsorption data on LiC at 77 K. The high-resolution data for each isothermal adsorption profile have been taken from Kruk and Jarioniec[29,30] for the two Ar isotherms and from Jaroniec et al.[31] for the N_2 isotherm. All three adsorption isotherms have shapes that are consistent with reversible, Type II physisorption on nonporous adsorbents.[3] Others have analyzed these published nitrogen and argon isotherms to test models for and seek understanding of adsorption processes on silica.[5,32−34]

Nitrogen at 77 K is frequently used for adsorption studies because it is easy to use, inexpensive, and unreactive toward most adsorbents. However, N_2 has a permanent quadrupole moment. Polarity on the adsorbent surface can affect the orientation of the N_2 adsorbate by inducing dipole/quadrupole interactions.[35] Argon is apolar, so adsorbate structures are not affected. Argon adsorption at 77 K can provide information on pore connectivity in ordered mesopore materials.[36] At this temperature, the Ar monolayer is affected by the adsorbent surface chemistry, so the liquefaction temperature of 87 K is preferred for BET specific area calculations.[3,37] Datar et al.[38] used grand canonical Monte Carlo simulations to show that calculated BET specific areas from N_2 and Ar isotherms are similar.

The adsorbent, LiC, is a macroporous, amorphous silica with no crystallinity apparent in X-ray diffraction patterns[39] and is used as a reference absorbent for the characterization of porous and modified silica.[40]

EXPERIMENTAL SECTION

High-Resolution Isothermal Adsorption Data. Measured capacities, $q_e(p)$, for Ar and N_2 adsorption on LiC taken from Kruk and Jaroniec[29,30] and Jaroniec et al.[31] have units μmole m^{-2}. That is, surface excess amount divided by the BET specific area of the adsorbent, S_B. For Ar adsorption at both 77 and 87 K, S_B is calculated to be 19.3 m^{-2} g^{-1},[29,30] and for N_2 at 77 K is 25.0 m^{-2} g^{-1}.[41]

Pressure-Varying Flexible Least-Squares (FLS) Methodology. Pressure-varying linear regression via FLS methodology for calculating universal Langmuir, $Q_{uL}(p)$ and $K_{uL}(p)$, and fractal parameters has been described in detail.[4,5] The parameters for each linear equation are assumed to vary slowly with increasing pressure and coverage and are calculated at each pressure via a five-point moving optimization of the data.[8] The FLS method involves ordinary linear regression for each set of five pressures and minimization of the sums of squared residuals for the dynamic change in the parameters with increasing pressure. The FLS code is reported by Kalaba and Tesfatsion[8] and has been adapted for the statistical computing language, R.[42]

Cost function, $C(p)$, is the sum of the residual ordinary linear regression errors and the residual dynamic errors. It would equal zero for an FLS analysis with no residual errors. Calculated cost functions for the universal Langmuir FLS calculations are listed in the Supplementary Information and are all close to zero, particularly at low pressures. Errors in FLS parameters are estimated from two standard deviations from the mean for five-point ordinary linear regression calculations. The mean error across all relative pressures up to 0.50, as a percentage

https://doi.org/10.1021/acs.langmuir.2c02932
Langmuir 2023, 39, 1914−1926

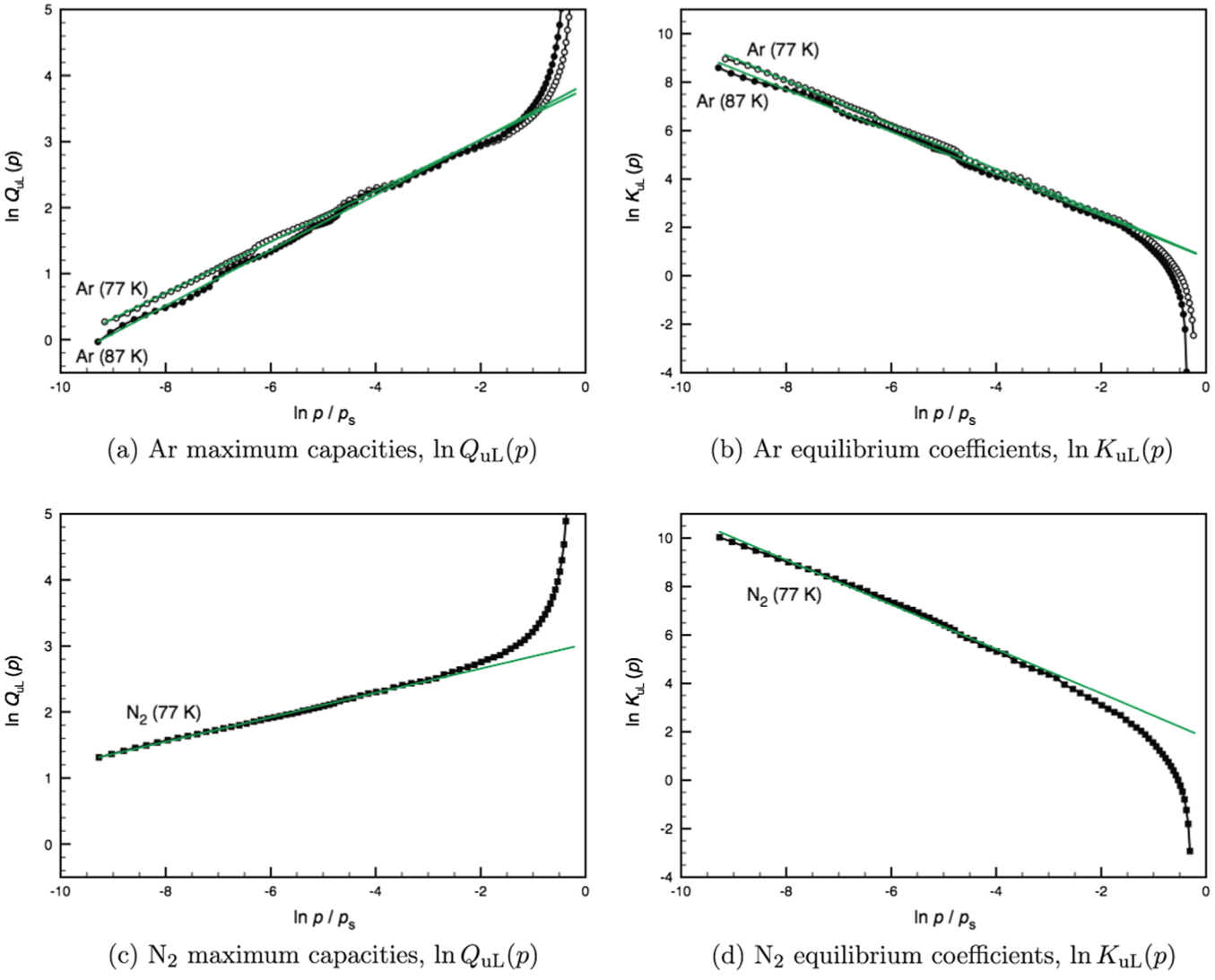

Figure 1. Logarithm of the universal Langmuir parameters for Ar at 77 K (open circles) and at 87 K (filled circles) in (a,b), and N_2 adsorption at 77 K (filled squares) on LiC in (c,d). Green, straight lines are linear regression fits to the data over the pressure ranges shown in Table 1.

of the parameters, are for Ar/LiC (77 K), 3.3 ± 1.2 %, for Ar/LiC (87 K), 3.7 ± 1.7 %, and for N_2/LiC (77 K), 5.0 ± 1.2 %. These optimal percentages are used to calculate and report errors in the universal Langmuir and fractal parameters.

RESULTS AND DISCUSSION

Universal Langmuir Parameters, $Q_{uL}(p)$ and $K_{uL}(p)$. Universal Langmuir parameters, $Q_{uL}(p)$ and $K_{uL}(p)$, are calculated using FLS and the linear form of eq 1:

$$\frac{1}{q_e(p)} = \frac{1}{Q_{uL}(p)} + \frac{1}{K_{uL}(p)\,Q_{uL}(p)}\,\frac{p_s}{p} \tag{6}$$

The logarithm of these universal Langmuir parameters for the Ar (77 K), Ar (87 K), and N_2 (77 K) adsorption isotherms on LiC are plotted against the logarithm of relative pressure in Figure 1. The shapes of the profiles are approximately linear up to $\ln p/p_s$ equals −2.54 for Ar (77 K), −2.53 for Ar (87K), and −2.67 for N_2 (77 K). Increasing maximum adsorption capacities are compensated by decreasing equilibrium adsorption capacities. At higher pressures, $\ln Q_{uL}(p)$ increases and $\ln K_{uL}$ decreases exponentially. As saturation pressures are neared, multilayers form and liquefaction or solidification occurs on the surface of the silica.

The linear regions at low pressures shown as green, straight lines in Figure 1 are power law distributions and are described by the following fractals for mean maximum adsorption capacities, $\overline{Q}_{uL}(p)$, and mean equilibrium adsorption coefficients, $\overline{K}_{uL}(p)$:

$$\ln \overline{Q}_{uL}(p) = \ln Q^{\circ}_{uL,F} + \gamma_1 \ln\left(\frac{p}{p_s}\right) \tag{7}$$

$$\ln \overline{K}_{uL}(p) = \ln K^{\circ}_{uL,F} + \gamma_2 \ln\left(\frac{p}{p_s}\right) \tag{8}$$

Here, $Q^{\circ}_{uL,F}$ and $K^{\circ}_{uL,F}$ are the mean fractals ($\overline{Q}_{uL}(p)$ and $\overline{K}_{uL}(p)$) extrapolated to p_s, while γ_1 and γ_2 are the respective fractal exponents. Listed in Table 1 are the resultant fractal parameters calculated over the specified pressure ranges.

Substituting the mean fractals from eqs 7 and 8 into the universal Langmuir eq 1 yields

https://doi.org/10.1021/acs.langmuir.2c02932
Langmuir 2023, 39, 1914−1926

Table 1. Fractal parameters from universal Langmuir parameters, $Q_{uL}(p)$ and $K_{uL}(p)$, from measured capacities, $q_e(p)$ and from adsorptive gas amounts, $q_{g,uL}(p)$. Adsorbate-dependent constants, c_e are from eq 18 and pressure-dependent coefficients, $c_e^*(p)$ from eq 21. Surface fractal dimensions, D_g are from eq 24. Errors are two standard deviations from the mean.

System	Ar/LiC (77 K)	Ar/LiC (87 K)	N_2/LiC (77 K)
ln p/p_s	-9.16 − -2.54	-9.29 − -2.53	-9.27 − -2.67
ln $Q^\circ_{uL,\,F}$ (μmole m^{-2})	3.80(3)	3.87(3)	3.029(16)
γ_1	0.387(4)	0.420(6)	0.185(2)
ln $K^\circ_{uL,\,F}$	0.75(5)	0.75(9)	1.75(13)
γ_2	-0.915(9)	-0.868(16)	-0.92(2)
ln $q^\circ_{e,\,F}$ (μmole m^{-2})	3.44(5)	3.57(6)	2.92(2)
γ_F	0.429(8)	0.497(10)	0.215(6)
c_e	1.10(2)	0.946(18)	2.19(6)
$c_e^*(p)$	1.45 + 0.062 ln (p/p_s)	1.36 + 0.076 ln (p/p_s)	3.2 + 0.15 ln (p/p_s)
ln $q^\circ_{g,\,uL,\,F}$ (μmole m^{-2})	2.69(5)	2.82(7)	1.15(11)
γ_g	0.339(8)	0.358(12)	0.123(18)
D_g	2.66(3)	2.64(8)	2.88(6)

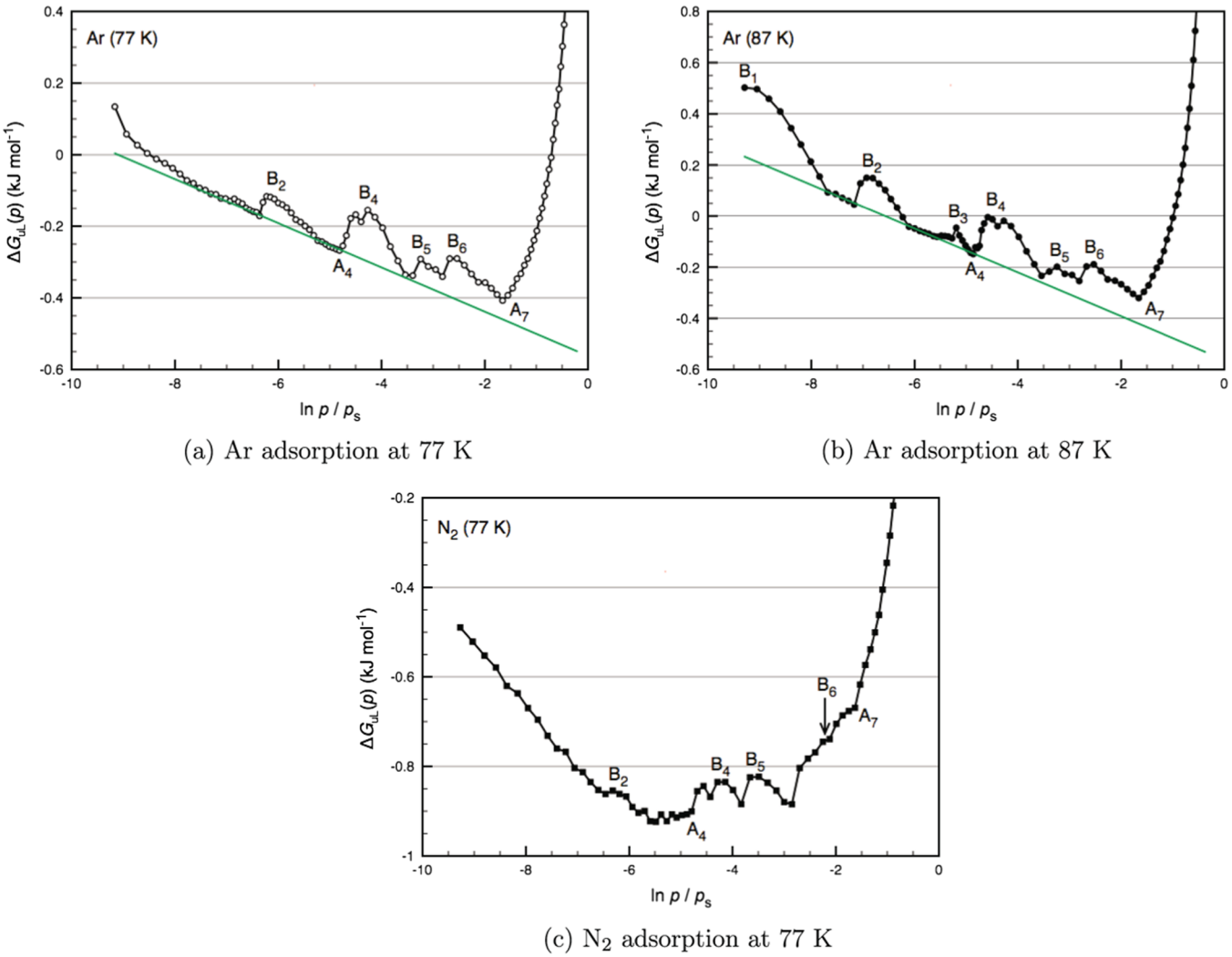

(a) Ar adsorption at 77 K

(b) Ar adsorption at 87 K

(c) N_2 adsorption at 77 K

Figure 2. Universal Langmuir Gibbs energy changes, $\Delta G_{uL}(p)$, for (a) Ar/LiC at 77 K, (b) Ar/LiC at 87 K, and (c) N_2/LiC at 77 K. Labels identify maxima (B_1 to B_6) and minima (A_4 and A_7). Green, straight lines are linear fits at minima, $\Delta G^*_{uL}(p)$.

$$q_e(p) = \frac{Q^\circ_{uL,F}\,(p/p_s)^{\gamma_1}\,K^\circ_{uL,F}\,(p/p_s)^{1+\gamma_2}}{1 + K^\circ_{uL,F}\,(p/p_s)^{1+\gamma_2}} \tag{9}$$

Equation 9 is equivalent to the four-parameter Baudu isotherm model[1,2] that has been shown to be an excellent fit to measured adsorption capacities. There have been limited reported applications of this model, and the physical significance of the parameters are not described.

Equations 2 and 3 indicate that the fractal exponents, γ_1 and γ_2, can be related to the Freundlich exponent, γ_F, from eq 5 and the fractal exponent, γ_g, associated with mean adsorptive gas amounts, $\overline{q}_{g,uL}$ (eq 23). That is,

https://doi.org/10.1021/acs.langmuir.2c02932
Langmuir 2023, 39, 1914−1926

$$\gamma_1 = \frac{\overline{q}_e(p)\,\gamma_F + \overline{q}_{g,uL}(p)\,\gamma_g}{\overline{Q}_{uL}(p)} \tag{10}$$

$$\gamma_2 = \gamma_F - \gamma_g \tag{11}$$

Thermodynamics of Adsorption. Universal Langmuir Gibbs energy changes of adsorption, $\Delta G_{uL}(p)$, may be determined from $K_{uL}(p)$ and eq 3:

$$\Delta G_{uL}(p) = -RT \ln K_{uL}(p)\, p/p_s = -RT \ln\left(\frac{q_e(p)}{q_{g,uL}(p)}\right) \tag{12}$$

Figure 2a,b are plots of $G_{uL}(p)$ against ln p/p_s for Ar adsorption at 77 and 87 K. Within each profile, there is an underlying, linear decline from positive to negative $G_{uL}(p)$ values. The empirical straight lines in Figure 2 highlight these apparent linear trends and the fitted equations are for Ar at 77 K:

$$\Delta G^*_{uL}(p) = -0.562 - 0.0618 \ln\left(\frac{p}{p_s}\right) \tag{13}$$

and for Ar at 87 K:

$$\Delta G^*_{uL}(p) = -0.563 - 0.0857 \ln\left(\frac{p}{p_s}\right) \tag{14}$$

Here, $\Delta G^*_{uL}(p)$ are minimum Gibbs energies associated with pressure-induced increases in the adsorbate density, uniformly distributed across the surface. With increases in pressure, the adsorptive gas density increases more relative to adsorbate density. Hence, adsorption becomes more favored.

Minimum enthalpy changes, $\Delta H^*_{uL}(p)$, and entropy changes, $\Delta S^*_{uL}(p)$, for single layer adsorption are calculated from eqs 13 and 14 at temperatures, T_1 and T_2, using:

$$\Delta H^*_{uL}(p) = \frac{T_2 \Delta G^*_{uL}(p, T_1) - T_1 \Delta G^*_{uL}(p, T_2)}{T_2 - T_1} \tag{15}$$

$$\Delta S^*_{uL}(p) = \frac{\Delta G^*_{uL}(p, T_1) - \Delta G^*_{uL}(p, T_2)}{T_2 - T_1} \tag{16}$$

Plots of $\Delta H^*_{uL}(p)$ and $\Delta S^*_{uL}(p)$ for Ar adsorption are shown in Figure 3. At the lowest pressures, both entropy and enthalpy changes are largest and negative. As adsorbate density increases, adsorbed Ar becomes more weakly adsorbed to the macroporous silica surface, while the less negative entropy indicates increasing ratios of adsorptive gas to adsorbate densities.

Peak variations from the straight lines in Figure 2a,b are labeled at B_1 to B_6. The maximal values of $\Delta G_{uL}(p)$ are given in Table S1. Optimal $\Delta H_{uL}(p)$ and $\Delta S_{uL}(p)$ values, for matching peaks using the $\Delta G_{uL}(p)$ values at 77 and 87 K, and eqs 15 and 16 are also listed. Small differences in pressure do not affect the thermodynamic values. Also in Table S1 are $\Delta H^*_{uL}(p)$ and $\Delta S^*_{uL}(p)$ optimum values at each labeled pressure, determined from eqs 15 and 16. The thermodynamic parameters for the troughs at A_4 and A_7 are also given in Table S1. For A_4, $\Delta H_{uL}(p) \approx \Delta H^*_{uL}(p)$ and $\Delta S_{uL}(p) \approx \Delta S^*_{uL}(p)$, indicating that the adsorbate structures at this pressure are uniformly distributed across the surface. For A_7, the $\Delta G_{uL}(p)$ minima is not close to the $\Delta G^*_{uL}(p)$ lines. This result suggests that at this pressure, there is a combination of structured adsorbate and liquid or solid layers. At higher pressures, the A_7 adsorbate structure transitions to liquid or solid Ar and the energetics become increasingly less favored.

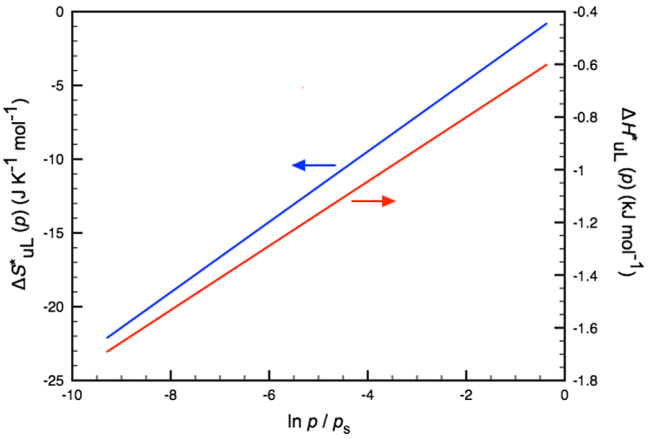

Figure 3. Mean universal Langmuir entropy changes (blue line) and enthalpy changes (red line) for Ar adsorption at 77 and 87 K from the $\Delta G^*_{uL}(p)$ empirical, straight lines shown in Figure 2a,b.

The peaks at B_1 to B_6 have less-favorable $\Delta G_{uL}(p)$ values when compared with $\Delta G^*_{uL}(p)$ at the same pressures. Those at B_2, B_4, B_5, and B_6 show more exothermic $\Delta H_{uL}(p)$ and more negative $\Delta S_{uL}(p)$ than the empirical minimum enthalpies and entropies. At each peak, there are increased and stronger adsorbate−adsorbate interactions and the density of adsorbed Ar increases via the formation of clusters. As the pressure increases, $\Delta G_{uL}(p)$ at the peak becomes more negative and adsorption becomes more favorable. This may indicate clusters that are dispersed and distributed more uniformly across the surface.

The $\Delta H_{uL}(p)$ and $\Delta S_{uL}(p)$ values at B_2 are large and negative. This suggests strong adsorbent−adsorbate bonding and the formation of clusters at specific sites (defects and holes) on the silica surface. The peak at B_1, only observed for Ar (87 K) adsorption, is also likely to correspond to strong bonding and clusters at specific adsorbent sites. Selective adsorption at 87 K is more sensitive to surface heterogeneity due to the higher kinetic energy Ar being mobile and able to access more of the surface.

The Gibbs energy profile for N_2 adsorption at 77 K shown in Figure 2c is much less resolved than for Ar at 77 and 87 K. Peaks (B_2 to B_6), trough (A_4), and an inflection (A_7) with adsorbate structures equivalent to the Ar structures can be identified. The optimal maxima, minimum, and inflection $\Delta G_{uL}(p)$ values for N_2 are all more favorable than for Ar. These are listed in Table S2. An underlying linear decrease in $\Delta G_{uL}(p)$ equivalent to the straight lines in Figure 2a,b cannot be identified.

Mean and Universal Fractals for Measured Capacities, $q_e(p)$. Plots of the logarithm of measured capacity, ln $q_e(p)$ against the logarithm of relative pressure are shown in Figure 4 for Ar and N_2 adsorption on LiC. High-resolution data were taken from Kruk and Jaroniec[29,30] and Jaroniec et al.[31] At low pressures, measured capacity is least for the Ar/LiC (87 K) isotherm and most for N_2/LiC (77 K). Lower Ar kinetic energies at 77 K cause adsorbate formation to be more favored than at 87 K, while the N_2 quadrupole moment[35] leads to stronger bonding with the silica surface. The three isotherms intersect at approximately p/p_s = 0.136 when $q_e(p)$ = 11.4 ± 0.3 μmole m^{-2}. At higher pressures, the logarithm of measured capacity curves upward corresponding to liquefaction or solidification.

Each of the plots in Figure 4 is approximately linear, up to relative pressures of 0.0789 at 77 K and 0.0797 at 87 K for Ar

https://doi.org/10.1021/acs.langmuir.2c02932
Langmuir 2023, 39, 1914−1926

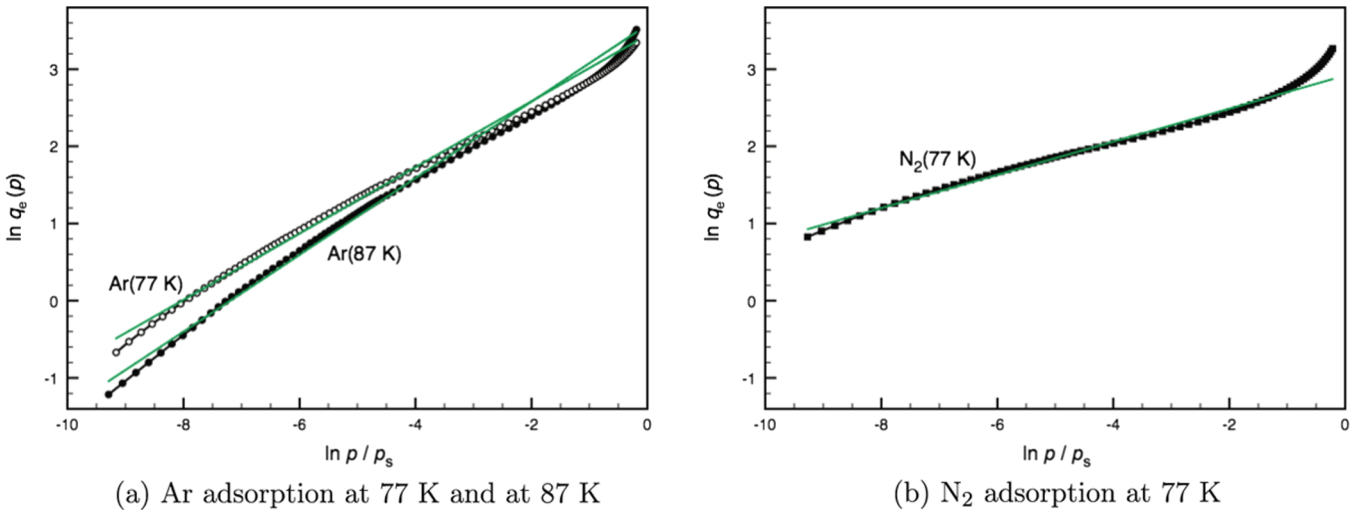

Figure 4. Logarithm of measured capacity, ln $q_e(p)$ plotted against the logarithm of relative pressure for Ar at 77 K (open circles) and 87 K (filled circles) in (a) and N_2 at 77 K (filled squares) on LiC in (b). Green lines are linear regression fits to the data at lower pressures.

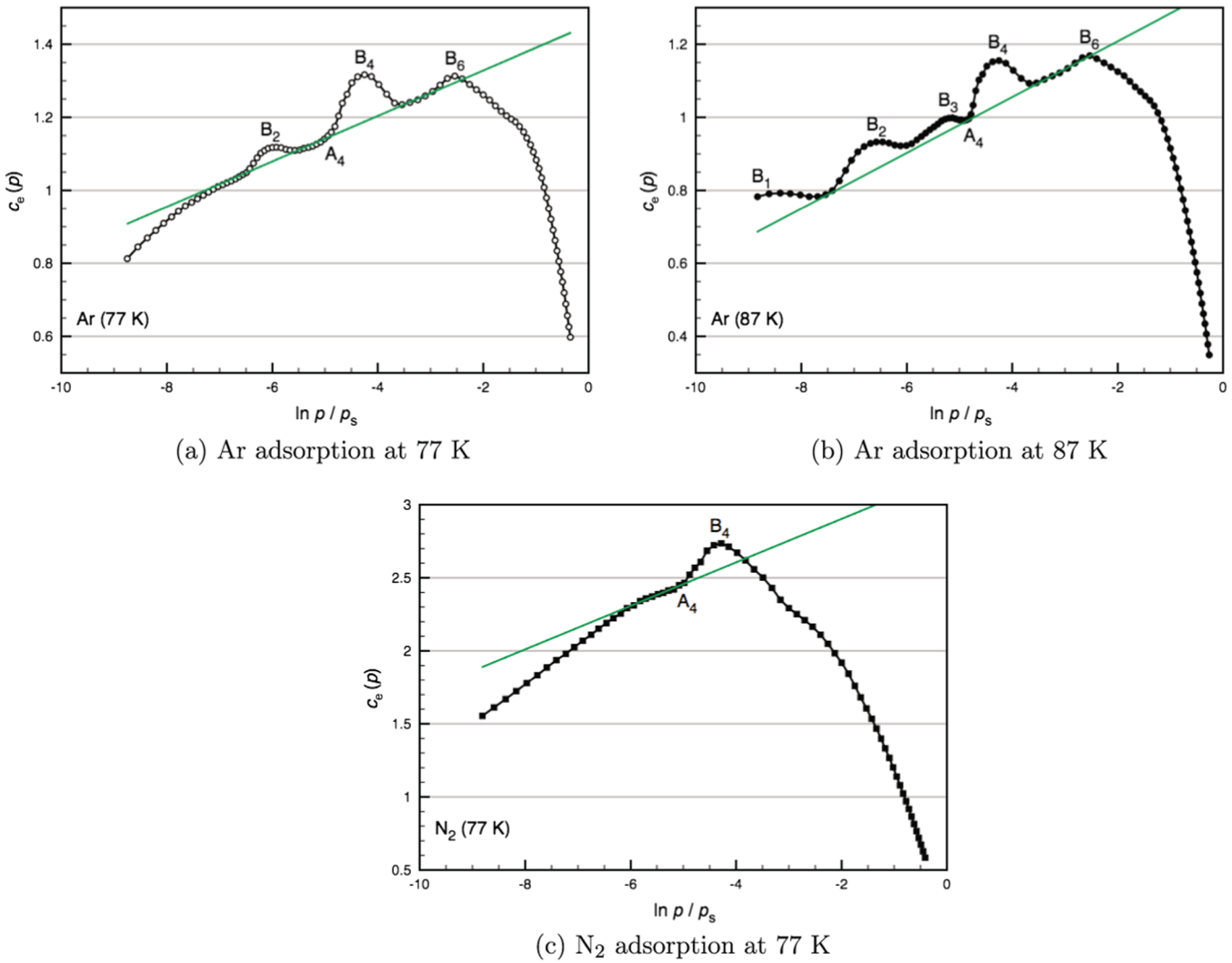

Figure 5. Pressure-varying fractal adsorbate coefficients, $c_e(p)$, for (a) Ar/LiC at 77 K, (b) Ar/LiC at 87 K, and (c) N_2/LiC at 77 K. Green lines show the linear increase, $c_e^*(p)$, at lower pressures. Labels, B_1 to B_6 and A_4, are at pressures where $c_e(p)$ values indicate different adsorbate structures.

adsorption and 0.0690 for N_2 at 77 K. Across these pressure ranges, the profiles are weakly curved with divergence from linearity most apparent at the lowest pressures. The straight lines in Figure 4 are the mean measured capacities, $\overline{q}_e(p)$, and are

https://doi.org/10.1021/acs.langmuir.2c02932
Langmuir 2023, 39, 1914−1926

described by the Freundlich eq 5, a power law distribution with fractal structures. Measured capacities extrapolated to p_s, $q^{\circ}_{e,F}$, and exponents, γ_F, are calculated by linear regression with eq 17.

$$\ln \overline{q}_e(p) = \ln q^{\circ}_{e,F} + \gamma_F \ln\left(\frac{p}{p_s}\right) \tag{17}$$

Resultant Freundlich or fractal parameters are listed in Table 1.

The fractal exponent, γ_F, is dependent on both the adsorbate and the adsorbent and can be related to the surface fractal dimension, D_e. Several relationships have been proposed.[25−27] The Atalay-Oral and Tatlier[27] model has the form $\gamma_F = (D_e - 1)/c_e$, where c_e is a constant dependent on the adsorbate. In order to calculate values of D_e that range between 2 and 3, equivalent to FHH (eq 4) surface fractal dimensions,[20] the following equation is used:

$$\gamma_F = \left(\frac{3 - D_e}{c_e}\right) \tag{18}$$

Here, c_e is the mean, effective adsorbate coverage over the linear pressure range. It is the coverage of adsorbate with access to the adsorbent surface and so available to probe adsorbent surface roughness. The magnitude of c_e can be estimated when D_e of the actual or a similar adsorbent is known.[25,27] The surface fractal dimension for N_2 adsorption on LiC at 77 K has been calculated, using random surface density functional theory and reported to be 2.53.[43] Substituting both this value and γ_F into eq 18 yields the c_e constants listed in Table 1 for each adsorption isotherm. The magnitude of c_e is smallest for Ar (87 K) and largest for N_2 (77 K) and is proportional to the trend in $q_e(p)$ as shown in Figure 4. Values of c_e = 0.946(18) for Ar at 87 K and 1.10(2) at 77 K, both close to unity, indicate that approximately single layers probe LiC surface roughness. The larger value of c_e = 2.19(6) for N_2 demonstrates that more than two N_2 layers are probing the silica surface.

Universal fractals from the measured adsorption capacities are determined by calculating Freundlich isotherm (eq 5) parameters, $q^{\circ}_{e,F}(p)$ and $\gamma_F(p)$, at each pressure. This is achieved using FLS and the linear expression:

$$\ln q_e(p) = \ln q^{\circ}_{e,F}(p) + \gamma_F(p) \ln\left(\frac{p}{p_s}\right) \tag{19}$$

In Figure S1a, the logarithm of each fractal capacity extrapolated to p_s, and $\ln q^{\circ}_{e,F}(p)$ are plotted for Ar at 77 and 87 K and N_2 at 77 K adsorption on LiC. The $\ln q^{\circ}_{e,F}(p)$ profiles are overall concave across the pressure ranges with smooth peaks and troughs at intermediate pressures. The fractal exponent, $\gamma_F(p)$, profiles in Figure S1b show approximately linear decreases up to the maximum relative pressures listed in Table 1. At higher pressures, $\gamma_F(p)$ increases steeply as saturation pressures are neared. Smooth peaks and troughs at low pressures are observed, analogous to Figure S1a.

The universal Freundlich exponents, $\gamma_F(p)$, are related to pressure-varying fractal adsorbate coverages, $c_e(p)$, and fractal dimension, D_e, of the silica surface from

$$\gamma_F(p) = \left(\frac{3 - D_e}{c_e(p)}\right) \tag{20}$$

By setting D_e = 2.53,[43] the reported LiC fractal dimension changes in $c_e(p)$ with increasing pressure can be investigated. Resultant profiles are shown in Figure 5 for Ar (77 K), Ar (87 K), and N_2 (77 K). For both Ar profiles, there is an underlying, linear increase in $c_e(p)$ with increasing $\ln p/p_s$ at low pressures. These trends are highlighted by the straight lines in Figure 5. A linear increase is less clear for N_2 (77 K), and the empirical, straight line in Figure 5c is fitted from the small range of increasing $c_e(p)$ coefficients at mid-range pressures. The empirical, linear equations for $c^*_e(p)$ have the form:

$$c^*_e(p) = c^{*\circ}_e + \gamma_c \ln\left(\frac{p}{p_s}\right) \tag{21}$$

Here, $c_e{}^{*\circ}$ is $c^*_e(p)$ extrapolated to saturation pressure and γ_c is the slope or exponent. The resultant empirical equations are included in Table 1. Linear $c^*_e(p)$ is indicative of ideal adsorption where adsorbate density increases uniformly and distributed across the surface with increases in pressure. Ideal adsorption where $c_e(p) \approx c^*_e(p)$ is the absence of pressure-induced transformations of adsorbate structure caused either by surface heterogeneity or adsorbate packing thermodynamics.

In Figure 5, values of $c_e(p)$ decrease steeply at higher pressures. As multilayers, liquid and solid formation dominates the adsorbate fraction with access to the surface and hence available to probe surface roughness decreases. This leads to a loss in sensitivity to transformations in adsorbate structures.

Fractal adsorbate coefficients at the lowest pressures for Ar (77 K) and for N_2 (77 K) are also less than $c^*_e(p)$. This suggests that the actual coverages and mobilities of adsorbed Ar and N_2 are insufficient to probe the complete silica surface. At these pressures and temperatures, adsorbates bind strongly to specific surface sites and do not diffuse across the surface to access all sites.

Variations from ideal adsorption are identified in Figure 5 by the peaks, B_1 to B_6. Here, Ar or N_2 form clusters. As pressure increases, $c_e(p)$ decreases from these peaks and Ar becomes more uniformly dispersed across the surface, i.e., $c_e(p) = c^*_e(p)$. For N_2, in Figure 5c, $c_e(p)$ values are significantly larger than for Ar and only B_4 is a clear peak. That is, N_2 is a less-sensitive probe than Ar of adsorbate structure transformations. Optimal $c_e(p)$ and $c^*_e(p)$ values at these peaks and for the ideal inflection point at A_4 are listed in Table S3.

The $c_e(p)$ peaks at B_1 (87 K only) and B_2 for Ar adsorption are linked to the formation of clusters at specific surface sites; defects, holes, or stronger-adsorbing sites. The $c_e(p)$ values at both B_1 and B_2 peaks for Ar (87K) are less than monolayer coverage, so the full surface is not accessed.

The small peak at B_3, only observed for Ar (87 K), is the start of a short series of adsorbate structures to A_4 where $c_e(p)$ = 1.00(4). That is, where Ar access remains monolayer, while adsorbate density increases as more Ar adsorbs. At A_4 for all isotherms, $c_e(p) = c^*_e(p)$, and are followed, at higher pressures by a sharp increase to B_4. Here, clusters form on top of the A_4 structures. The very small peaks at B_6 for Ar (77 K) and Ar (87 K) in Figure 5 are at the end of the empirical lines and the start of the steep fall-off in $c_e(p)$.

Mean and Pressure-Varying Fractals for the Adsorptive Gas, $q_{g,uL}(p)$. Amounts of adsorptive gas, $q_{g,uL}(p)$, are calculated from the universal Langmuir parameters, $Q_{uL}(p)$ and $K_{uL}(p)$, by combining eqs 2 and 3:

$$q_{g,uL}(p) = \frac{Q_{uL}(p)}{K_{uL}(p)\, p/p_s + 1} \tag{22}$$

https://doi.org/10.1021/acs.langmuir.2c02932
Langmuir 2023, 39, 1914−1926

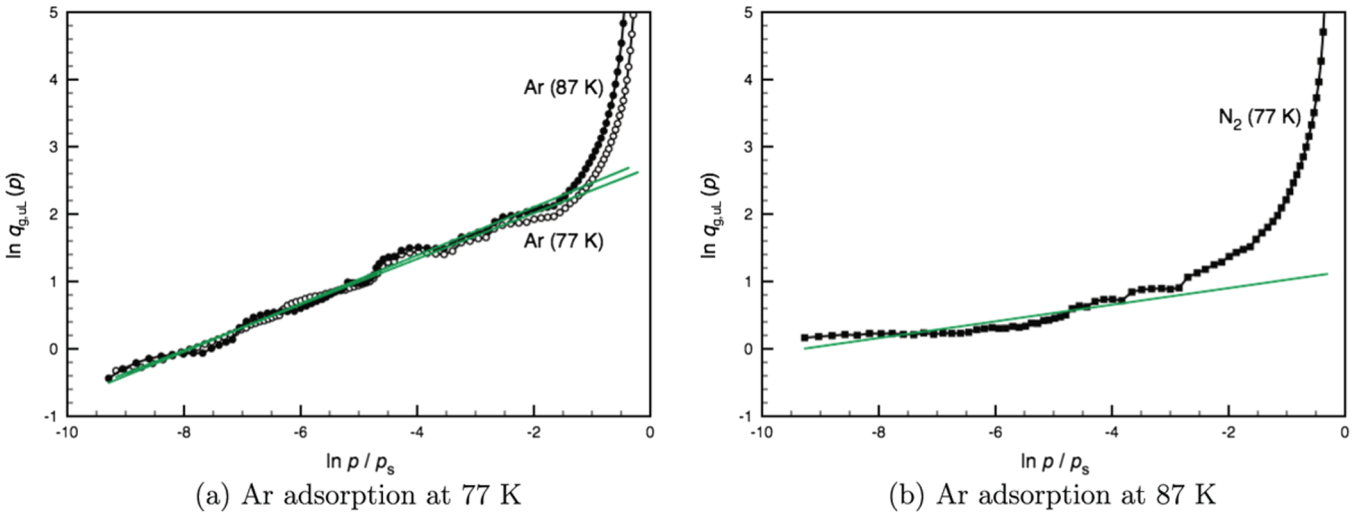

Figure 6. Pressure-varying adsorptive gas amounts, $q_{g,uL}(p)$, for Ar at 77 K (open circles) and 87 K (filled circles) in (a), and N_2 at 77 K (filled squares) on LiC in (b). Green lines are linear fits to the data at lower pressures.

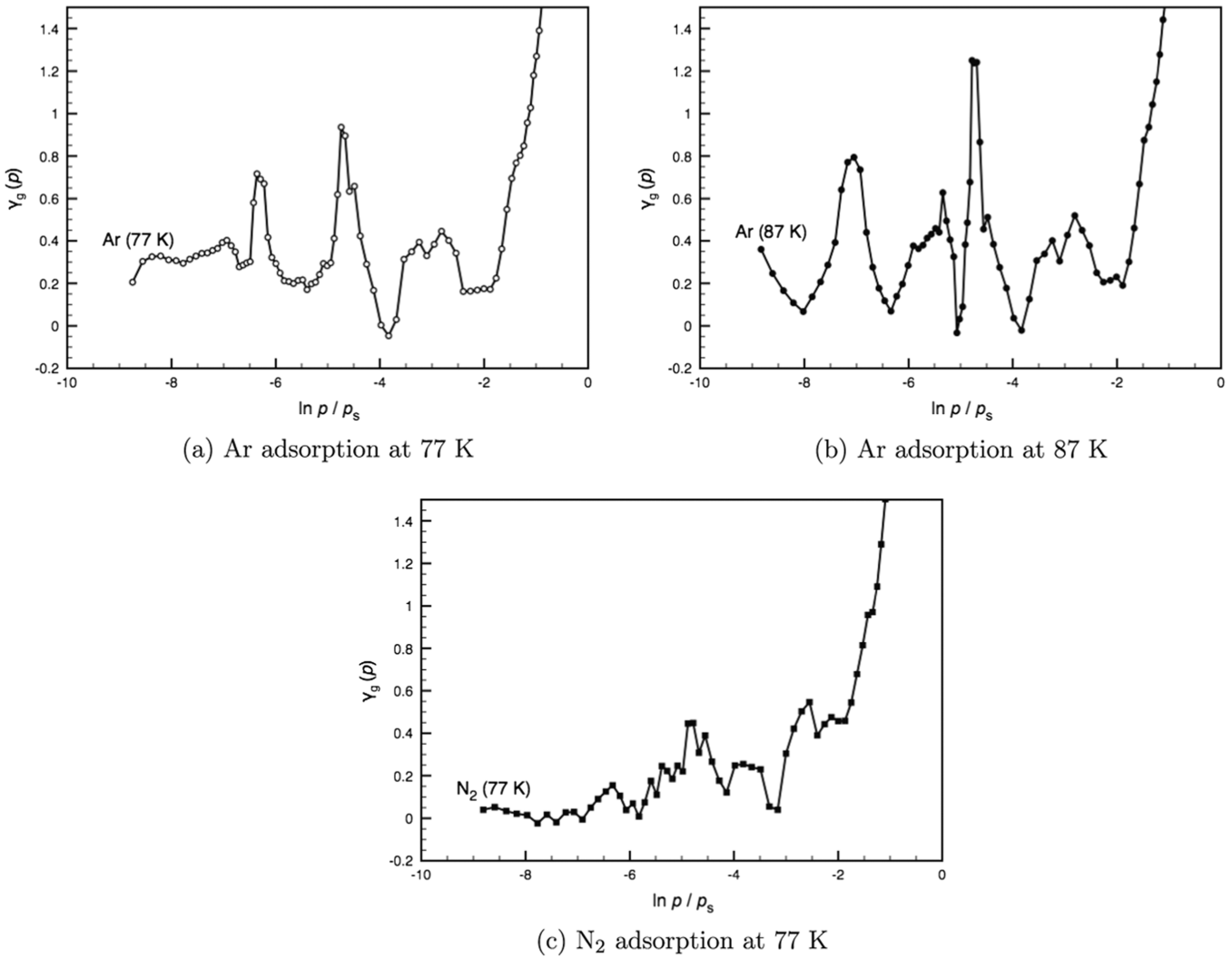

Figure 7. Pressure-varying fractal exponents, $\gamma_g(p)$, from pressure-varying Langmuir adsorptive gas amounts for (a) Ar/LiC at 77 K, (b) Ar/LiC at 87 K, and (c) N_2/LiC at 77 K.

In Figure 6, $\ln q_{g,uL}(p)$ for each of the adsorption isotherms is plotted against $\ln p/p_s$.

The linear fits at low pressures in Figure 6 are the mean fractals, $\ln \overline{q}_{g,uL}(p)$, for the adsorptive gas:

https://doi.org/10.1021/acs.langmuir.2c02932
Langmuir 2023, 39, 1914−1926

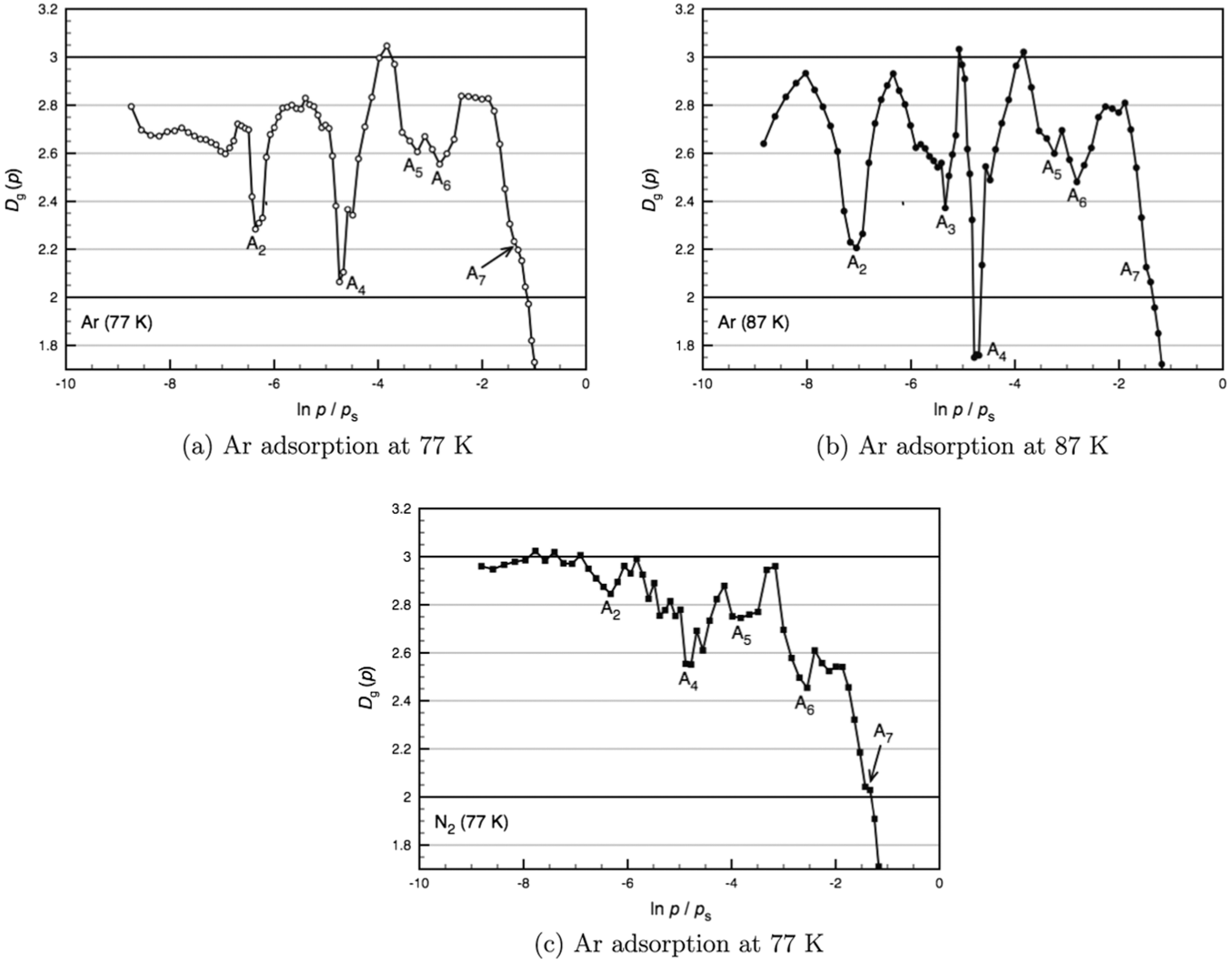

(a) Ar adsorption at 77 K (b) Ar adsorption at 87 K

(c) Ar adsorption at 77 K

Figure 8. Pressure-varying fractal dimensions, $D_g(p)$, from universal Langmuir adsorptive gas amounts. Labels along the $D_g(p)$ profiles identify minima (A_2 to A_6) and an inflection (A_7) for (a) Ar/LiC at 77 K, (b) Ar/LiC at 87 K, and (c) N_2/LiC at 77 K.

$$\ln \overline{q}_{g,uL}(p) = \ln q^{\circ}_{g,uL,F} + \gamma_g \ln\left(\frac{p}{p_s}\right) \tag{23}$$

where $q^{\circ}_{g,\,uL,\,F}(p)$ is the extrapolated adsorptive gas amount at p_s and $\gamma_g(p)$ is the fractal exponent. Resultant fractal parameters are listed in Table 1. For Ar at 77 and 87 K, the fractals are good fits to the data in Figure 6 throughout the specified pressure ranges. However, for N_2, the profile is concave so the mean fractal is not as true a fit.

The magnitude of the exponent, γ_g, is sensitive to and directly proportional to the mean fractal dimension, D_g, of the combined adsorbate and adsorbent surface. The following, analogous to eq 18 is used to calculate values of D_g that can range between 2 and 3::[20]

$$\gamma_g = \left(\frac{3 - D_g}{c_g}\right) \tag{24}$$

Here, c_g is the mean proportion of the adsorptive gas with access to the surface and is set equal to unity. This is because it is assumed that all the adsorptive gas has access to the surface. Resultant values of D_g for each of the isotherms are included in Table 1. For Ar, the combined adsorbate and adsorbent surface roughness is equal, 2.66(3) at 77 K and 2.64(8) at 87 K. For N_2, D_g is larger at 2.88(6) hence approaching maximum roughness (3.0). The reported, theroretical surface fractal dimension for pure LiC from N_2 adsorption at 77 K on LiC at 77 K is 2.53.[43] As expected, apparent surface roughness is enhanced by adsorbed Ar and N_2.

In order to investigate deviations from the linear $\ln \overline{q}_{g,uL}(p)$ (straight lines in Figure 6), pressure-varying fractal parameters are calculated using FLS and the fractal:

$$\ln q_{g,uL}(p) = \ln q^{\circ}_{g,uL,F}(p) + \gamma_g(p) \ln\left(\frac{p}{p_s}\right) \tag{25}$$

Here, $q^{\circ}_{g,\,uL,\,F}(p)$ is the extrapolated adsorptive gas amounts at p_s and the fractal exponents are $\gamma_g(p)$ at each pressure. Calculated values of $\gamma_g(p)$ are plotted in Figures 7a,b for Ar at 77 and 87 K and in Figure 7c for N_2 at 77 K. The $q^{\circ}_{g,\,uL,\,F}(p)$ profiles match the $\gamma_g(p)$ structures of peaks, troughs, and inflections.

As with eq 24, the magnitudes of the fractal exponents, $\gamma_g(p)$, are sensitive to and directly proportional to the fractal dimensions, $D_g(p)$, of the combined adsorbate and adsorbent surface and inversely proportional to the accessible fraction of the adsorptive gas, c_g:

https://doi.org/10.1021/acs.langmuir.2c02932
Langmuir 2023, 39, 1914−1926

$$\gamma_g(p) = \left(\frac{3 - D_g(p)}{c_g}\right) \tag{26}$$

By setting c_g = 1.0 and independent of pressure, temperature, and adsorptive gas, $D_g(p)$ may be estimated for the pressure-varying adsorbate structures. Resultant values of $D_g(p)$ are plotted against ln p/p_s in Figure 8a,b for Ar adsorption at 77 and 87 K and in Figure 8c for N_2 (77 K). Peaks where there is maximum surface roughness, $D_g(p) \approx 3$, for Ar (87 K) are associated with the B_1 to B_4 peaks, labeled in Figures 2b and 5b. For Ar (87 K) $D_g(p) \approx 3$ at B_4. For N_2 adsorption in Figure 8c, adsorbate clusters at low pressures lead to maximum surface roughness.

Troughs, A_2 to A_6, are labeled in Figure 8. These sharp minima precede each B_2 to B_6 peak and indicate that the adsorbate structures at these pressures cause surface smoothing. Minimum values of $D_g(p)$ are listed in Table S4. The value of $D_g(p)$ at A_4 for Ar (87 K) is 1.75(6) or less than 2, which is not meaningful. For a smooth 2-dimensional surface ($D_g(p) = 2.00$), the value of c_g would need to be adjusted to 0.804(8). For Ar (77 K), $D_g(p)$ = 2.06(7) at A_4 is also indicative of smooth surface. The shallow A_4 trough for N_2 (77 K) is $D_g(p)$ = 2.55(13), indicating that the adsorbate at this pressure matches the roughness of the pure silica.

The shallow troughs at A_3 (Ar (87 K) only), A_5 and A_6 show transitions to adsorbate structures with some surface smoothing. The structures at A_2 cause significant smoothing for Ar at both 77 and 87 K and may be associated with the filling of defects or holes in the LiC surface. For N_2, this A_2 trough is shallow.

Inflection points at A_7 are associated with transitions from multiple layers to liquid or solid formation.

Universal Langmuir Specific Area. The sharp, large troughs for $D_g(p)$ at A_4 in Figure 8 are identified as the pressures where the adsorbates form a monolayer of close-packed or BET structures. That is, where the cross-sectional area of each adsorbate atom of molecule is $a_{m,B}$ (13.8 Å^2 for Ar and 16.2 Å^2 for N_2). Values of $D_g(p)$ near 2.0 indicate smooth adsorbate structures at these pressures. Villiéras et al.[44] have proposed that close-packed BET structures are smooth and may not follow the surface topography. Furthermore, $\Delta G^\circ_{uL}(p)$ at A_4 in Figure 2 is close to the minima prior to B_4 peaks and so are thermodynamical favored adsorbate structures.[16] The $\Delta H^\circ_{uL}(p)$ and $\Delta S^\circ_{uL}(p)$ values at A_4 in Table S1 are less negative than the B_4 enthalpy and entropy changes. This indicates that Ar is more weakly adsorbed on the surface and more evenly distributed across the surface at A_4 pressures.

The universal Langmuir specific area, S_{uL}, of LiC is calculated from the BET specific area, S_B, the BET maximum adsorption capacity, Q_B, and the universal Langmuir maximum adsorption capacity at A_4, Q_{uL,A_4}:

$$S_{uL} = \frac{S_B\, Q_{uL,A_4}}{Q_B} \tag{27}$$

Calculated values of Q_B, S_B, Q_{uL,A_4} and S_{uL} are listed in Table 2.

The magnitudes of S_{uL} vary significantly for the three systems and are less than the BET specific areas. The former contradicts grand canonical Monte Carlo calculations that indicate BET specific areas from N_2 and Ar isotherms are similar.[38] Table S4 shows that for Ar (87 K) $c_e(p) = c_e^*(p)$ = 1.00(4) at A_4. This suggests that for this system and at this pressure, Ar is packed as a complete Ar monolayer on the surface. Hence, $S_{uL,Ar(87\ K)}$ = 10.1(4) m^2 g^{-1} can be considered to be the true specific area. For Ar (77 K), $c_e(p)$ = 1.22(4) and $c_e^*(p)$ = 1.16(10) at A_4, while for N_2 (77 K), $c_e(p)$ = 2.57 and $c_e^*(p)$ = 2.49. These nonunity values indicate that for both isotherms, monolayers are exceeded and the average space accessed by each Ar or N_2 is greater than $a_{m,B}$ at A_4 pressures. Pressure-varying BET coverages, $c_{e,B}(p)$, are where the absorbate cross-sectional areas are constant and equal to $a_{m,B}$. These are calculated from:

$$c_{e,B}(p) = \frac{Q_{uL}(p)}{Q_{uL,A_4}} \times \frac{S_{uL}}{S_{uL,Ar(87K)}} \tag{28}$$

Here, Q_{uL,A_4} is the maximum adsorption capacity at A_4 for each isotherm. Values of $c_{e,B}(p)$ for the labeled, B_1 to B_6 and A_2 to A_7, are listed in Table S5. At A_4, $c_{e,B}(p) = S_{uL}/S_{uL,Ar(87\ K)}$, and equals 1.15(4) for Ar (77 K), 1.00(4) for Ar (87 K), and 2.02(10) for N_2 (77 K). These are the number of layers of absorbate at A_4 pressures. For Ar (77 K), $c_{e,B}(p) \approx c_e^*(p)$ and $c_e(p)$ is 6% larger indicating some mobility of the Ar. For N_2 (77 K), $c_{e,B}(p) < c_e(p) \approx c_e^*(p)$. At A_4 pressures, N_2 is mobile and each molecule in the two layers accesses an additional 26% of the surface. Higher mobility may only refer to adsorbate in the second layer

Values of $a_e(p)$, the average space accessed by each adsorbed Ar or N_2, are determined from:

$$a_e(p) = \frac{a_{m,B}\, c_e(p)}{c_{e,B}(p)} \tag{29}$$

where $c_e(p)$ is the apparent coverages listed in Tables S3 and S4. Values for $c_{e,B}(p)$ and adsorbate atomic and molecular areas, $a_e(p)$, for each of the structures (B_1 to B_6 and A_2 to A_7) are given in Table S5. Also included in Table S5 are $a_m^*(p)$ values calculated with $c_e^*(p)$ in place of $c_e(p)$ in eq 29.

Adsorbate Structures: A_2 to A_7. The A_2 to A_7 structures are at pressures where $D_g(p)$ are troughs in Figure 8 and 8c indicating smoothing of the surface caused by adsorbed Ar or N_2. In Figure 5, they are at pressures where $c_e(p) \approx c_e^*(p)$, and where $\Delta G^\circ_{uL}(p) \approx \Delta G_{uL}{}^{\circ *}(p)$ in Figure 2. Each A_2 to A_6 structure is more favored than the subsequent B_2 to B_6 structure. Both enthalpy and entropy changes are also less negative than the subsequent B structure.

The A_2 structure is in all three isotherms although is at a lower pressure for Ar (87 K), while the A_3 structure is only observed for Ar (87 K). Increased smoothing is apparent for Ar at A_2 pressures ($D_g(p)$ is 2.28(8) (77 K) and 2.21(8) (87 K)) and at A_3 pressure ($D_g(p)$ is 2.37(9) (87 K)). There is also a local increase in smoothing for N_2 (2.84(14)) at A_2. This suggests that these adsorbate structures are filling defects or holes in the silica surface. Incomplete coverages, $c_{e,B}(p)$, for both Ar systems and large values of $a_e(p)$ indicate vacant surface sites. For Ar (87 K), $a_e(p) > a_e^*(p)$, showing increased adsorbate access and mobility at this temperature. The stronger surface sites are filled at lower pressures. For N_2 (77 K), $c_{e,B}(p)$ = 1.53(8), so the surface smoothing in Figure 8c caused by filling of defects or holes is

Table 2. Calculated Values of Q_B, S_B, Q_{uL,A_4} and S_{uL} from Eq 27

system	Ar/LiC (77 K)	Ar/LiC (87 K)	N_2/LiC (77 K)
Q_B (μmole m^{-2})	12.03	12.03	10.25
S_B (m^{-2} g^{-1})	19.3[29]	19.3[30]	25.0[41]
Q_{uL,A_4} (μmole m^{-2})	7.2(2)	6.3(2)	8.4(4)
S_{uL} (m^{-2} g^{-1})	11.6(4)	10.1(4)	20.5(1.0)

https://doi.org/10.1021/acs.langmuir.2c02932
Langmuir 2023, 39, 1914−1926

obscured by the roughness caused by a disordered monolayer of absorbate.

The A_3, A_4, A_5, and A_6 structures are all likely to have ordered, adsorbate packing distributed across the surface. For A_3, only observed for Ar (87 K), $D_g(p) = 2.37(9)$, $c_{e,B}(p) = 0.81(3)$, $a_e(p) = 16.8$ Å^2, and $a_e(p) > a_e^*(p)$. That is, there are vacant sites and some mobile, nonpacked Ar is causing roughness on the surface. For A_5 and A_6, there are small, local increases in surface smoothness and $a_e(p) = a_e^*(p)$ for all isotherms, except for N_2 (77 K) at A_6 pressure where $a_e(p) < a_e^*(p)$. This last is because the $c_e(p)$ does not include adsorbed N_2, not in direct contact with the silica. Argon coverages, $c_{e,B}(p)$, are 1.95(7) at A_5 and 2.22(8) at A_6, while the N_2 coverage is 2.45(12) at A_5 pressure. The first layers may have the close-packed BET structures, while the second and subsequent layers have structures that are disordered and distributed across the surface.

The A_7 pressure is likely to be where the ordered, adsorbate in direct contact with the silica surface, transitions to a disordered, mobile liquid or solid structure. For all three adsorption systems, $a_e(p) < a_e^*(p)$, because the calculated $c_e(p)$ are less than the true values.

Adsorbate Structures: B_1 to B_6. The B_1 to B_6 adsorbate structures are apparent at pressures soon after the corresponding A structure. The B_1 structure is only in the Ar (87 K) profiles, and pressures are not sufficiently low to observe a preceding A_1 structure. All $D_g(p)$ values for the B_1 to B_6 structures, plotted in Figure 8, indicate increases in surface roughness. Also, $\Delta G_{uL}(p) > \Delta G_{uL}^*(p)$ in Figure 2. That is, adsorption is less favored than for the corresponding A structure with more negative $\Delta H_{uL}(p)$ and $\Delta S_{uL}(p)$ for the Ar systems. For B_1 to B_5, $a_e(p) > a_e^*(p)$, while for B_6, $a_e(p) = a_e^*(p)$. The B_6 peaks in Figure 5 are very small and are a combination of structured adsorbate and liquid or solid layers.

Each B_1 to B_6 structure is assigned to the formation of disordered clusters of Ar or N_2 on top of the lower-pressure A structure. When the pressure is increased further, the clusters disperse to more-ordered structures across the surface.

CONCLUSIONS

Detailed universal Langmuir and fractal analyses of the high-resolution adsorption isotherms of Ar at 77 and 87 K and N_2 at 77 K on macroporous silica have yielded new insights. Most significant are apparent transformations of the adsorbate structure caused by changes to the adsorptive gas pressure and coverage. These transformations are evident in plots of $\Delta G_{uL}(p)$ against $\ln p/p_s$ with series of broad peaks where adsorption is less favored. For the Ar isotherms, both $\Delta H_{uL}(p)$ and $\Delta S_{uL}(p)$ are more negative at the peaks than the values for uniform adsorbate packing. Broad peaks are also apparent in plots of fractal adsorbate coefficients, $c_e(p)$, against $\ln p/p_s$. Sharper peaks and troughs, associated with adsorbate structural transformations, are observed for pressure-varying fractal dimensions, $D_g(p)$, calculated from universal Langmuir adsorptive gas amounts. Fluctuations in D_g indicate that there are specific pressures and coverages where the combined adsorbate and adsorbent appears rougher and other regions where it appears smoother. The Ar (87 K) isotherm is most sensitive to transformations to the adsorbate structure, while the N_2 (77 K) isotherm is least sensitive. These variations in sensitivity are due to N_2 having a permanent quadrupole moment, while Ar is apolar, and because 87 K is the liquefaction temperature of Ar.

In order to confirm the adsorbate structural transformations future work needs to explore the effects of other adsorbates and adsorbents on the apparent transformations. Furthermore, adsorption on micro- or mesoporous materials is expected to produce isotherms where the adsorbate structures observed for macroporous materials are obscured by the filling of the pores. This limitation may be restricted to narrow pressure ranges for some adsorbents and needs to be investigated.

Adsorbate structures that are dependent on pressure and coverage include the filling of defects and holes on the silica surface, cluster formation, and adsorbed Ar or N_2 uniformly distributed or packed across the surface. One of the sharp troughs observed in all of the D_g plots corresponds to a smooth surface and is associated with close-packed Ar or N_2. For Ar (87 K) the adsorbate structure is a monolayer (1.00(4)) and gives a universal Langmuir specific area of 10.1(4) m^2 g^{-1}. For Ar (77 K) the coverage at this trough is 1.15(4) layers and for N_2 at 87 K, it is 2.02(10) layers.

ASSOCIATED CONTENT

Supporting Information

The Supporting Information is available free of charge at https://pubs.acs.org/doi/10.1021/acs.langmuir.2c02932.

Table S1: Optimal universal Langmuir thermodynamic parameters for Ar/LiC at 77 and 87 K; Table S2: Optimal universal Langmuir thermodynamic parameters for N2/LiC at 77 K; Figure S1: Universal fractal parameters from measured capacities for Ar/LiC at 77 and 87 K and N2/LiC at 77 K; Table S3: Optimal adsorbate fractal coverages for Ar/LiC at 77 and 87 K and N2/LiC at 77 K; Table S4: Optimal adsorbate surface fractal dimensions for Ar/LiC at 77 and 87 K and N2/LiC at 77 K; Table S5: Optimal adsorbate fractal BET coverages and cross-sectional areas for Ar/LiC at 77 and 87 K and N2/LiC at 77 K; Table S6: Universal Langmuir maximum capacities, equilibrium coefficients, and cost functions for the Ar/LiC at 77 K; Table S7: Universal Langmuir maximum adsorption capacities, equilibrium adsorption coefficients, and cost functions for the Ar/LiC isotherm at 87 K (PDF)

AUTHOR INFORMATION

Corresponding Author

Trevor C. Brown − *Chemistry, School of Science and Technology, University of New England, Armidale, NSW 2351, Australia;* orcid.org/0000-0002-8277-2498; Email: tbrown3@une.edu.au

Authors

Ali Bagheri − *Chemistry, School of Science and Technology, University of New England, Armidale, NSW 2351, Australia;* orcid.org/0000-0003-3484-5856

Christopher M. Fellows − *Desalination Technologies Research Institute, Al Jubail 31951, Saudi Arabia; Chemistry, School of Science and Technology, University of New England, Armidale, NSW 2351, Australia*

Complete contact information is available at: https://pubs.acs.org/10.1021/acs.langmuir.2c02932

Notes

The authors declare no competing financial interest.

■ ACKNOWLEDGMENTS

The authors thank Professor David Miron, University of New England, for the suggestion to use FLS and for other computational advice.

■ REFERENCES

(1) Majd, M. M.; Kordzadeh-Kermani, V.; Ghalandari, V.; Askari, A.; Sillanpä, M. Adsorption isotherm models: A comprehensive and systematic review (2010−2020). *Sci. Total Environ.* **2021**, *812*, No. 151334.
(2) Rajahmundry, G. K.; Garlapati, C.; Kumar, P. S.; Alwi, R. S.; Vo, D. V. N. Statistical analysis of adsorption isotherm models and its appropriate selection. *Chemosphere* **2021**, *276*, No. 130176.
(3) Thommes, M.; Kaneko, K.; Neimark, A. V.; Olivier, J. P.; Rodrihuez-Reinoso, F.; Rouquerol, J.; Sing, K. S. W. Physical adsorption characterization of manoporous materials. *Pure Appl. Chem.* **2015**, *87*, 1051−1069.
(4) Brown, T. C. Adsorption properties from pressure-varying Langmuir parameters: nbutane and isobutane on activated carbon. *Energy Fuels* **2017**, *31*, 2109−2117.
(5) Brown, T. C.; Miron, D. J.; Fellows, C. M. Pressure-varying Langmuir parameters and stepped nitrogen adsorption on alumina and silica. *Phys. Chem. Chem. Phys.* **2019**, *21*, 2558−2566.
(6) Langmuir, I. The adsorption of gases on plane surfaces of glass, mica and platinum. *J. Am. Chem. Soc.* **1918**, *40*, 1361−1403.
(7) Bian, L.; Shi, P. An improved isothermal adsorption equation of gaseous molecules under low pressure in gas-solid system. *J. Phase Equilib. Diffus.* **2018**, *39*, 117−128.
(8) Kalaba, R.; Tesfatsion, L. Time-varying linear regression via flexible least squares. *Comput. Math. Appl.* **1989**, *17*, 1215−1245.
(9) Azizian, S.; Eris, S.; Wilson, L. Re-evaluation of the century-old Langmuir isotherm for modeling adsorption phenomena in solution. *Chem. Phys.* **2018**, *513*, 99−104.
(10) Chang, C. K.; Chen, C. C. An activity-based formulation for Langmuir adsorption isotherm. *Adsorption* **2020**, *26*, 375−386.
(11) Laaksonen, A. A unifying model for adsorption and nucleation of vapors on solid surfaces. *J. Phys. Chem. A* **2015**, *119*, 3736−3745.
(12) Narayanaswamy, N.; Ward, C. A. Specific surface area, wetting, and surface tension of materials from N_2 vapor adsorption isotherms. *J. Phys. Chem. C* **2019**, *123*, 18336−18346.
(13) Buttersack, C. Modeling of type IV and V sigmoidal adsorption isotherms. *Phys. Chem. Chem. Phys.* **2019**, *21*, 5614−5626.
(14) Haiss, W. Surface stress of clean and adsorbate-covered solids. *Rep. Prog. Phys.* **2001**, *64*, 591−648.
(15) Gor, G. Y.; Huber, P.; Bernstein, N. Adsorption-induced deformation of nanoporous materials - A review. *Appl. Phys. Rev.* **2017**, *4*, No. 011303.
(16) Shimizu, S.; Matubayasi, N. Surface Area Estimation: Replacing the Brunauer − Emmett − Teller Model with the Statistical Thermodynamic Fluctuation Theory. *Langmuir* **2022**, *38*, 7989−8002.
(17) Park, J.; Howe, J. D.; Sholl, D. S. How reproducible are isotherm measurements in metal-organic frameowrks. *Chem. Mater.* **2017**, *29*, 10487−10495.
(18) Ismail, I. M. K.; Pfeiffer, P. Fractal analysis and surface roughness of nonporous carbon fibers and carbon blacks. *Langmuir* **1994**, *10*, 1532−1538.
(19) Sahouli, B.; Blacher, S.; Brouers, F. Applicability of the Fractal FHH Equation. *Langmuir* **1997**, *13*, 4391−4394.
(20) Avnir, D.; Jaroniec, M. An isotherm equation for adsorption on fractal surfaces of heterogeneous porous materials. *Langmuir* **1989**, *5*, 1431−1433.
(21) Brown, J. H.; Gupta, V. K.; Li, B.-L.; Milne, B.; Restrepo, C.; West, G. B. The fractal nature of nature: power laws, ecological complexity and biodiversity. *Philos. Trans. R. Soc. London, Ser. B* **2002**, *357*, 619−626.
(22) Freundlich, H. M. F. Over the adsorption in solution. *J. Phys. Chem.* **1906**, *57*, 385−471.
(23) Kanô, F.; Abe, I.; Kamaya, H.; Ueda, I. Fractal model for adsorption on activated carbon surfaces: Langmuir and Freundlich adsorption. *Surf. Sci.* **2000**, *467*, 131−138.
(24) Ehrburger-Dolle, F. Analysis of the Derived Curves of Adsorption Isotherms. *Langmuir* **1997**, *13*, 1189−1198.
(25) Tatlier, M.; Erdem-Senatalar, A. Method to Evaluate the Fractal Dimensions of Solid Adsorbents. *J. Phys. Chem. B* **1999**, *103*, 4360−4365.
(26) Passe-Coutrin, N.; Altenor, S.; Cossement, D.; Jean-Marius, C.; Gaspard, S. Comparison of parameters calculated from the BET and Freundlich isotherms obtained by nitrogen adsorption on activated carbons: A new method for calculating the specific surface area. *Microporous Mesoporous Mater.* **2008**, *111*, 517−522.
(27) Atalay-Oral, C.; Tatlier, M. Characterization of mixed matrix membranes by adsorption and fractal analysis. *Sep. Sci. Technol.* **2019**, *54*, 2323−2333.
(28) Villiéras, F.; Michot, L. J.; Bardot, F.; Chamerois, M.; Eypert-Blaison, C.; François, M.; Gérard, G.; Cases, J.-M. Surface heterogeneity of minerals. *C. R. Geosci.* **2002**, *334*, 597−609.
(29) Kruk, M.; Jaroniec, M. Determination of Mesopore Size Distributions from Argon Adsorption Data at 77 K. *J. Phys. Chem. B* **2002**, *106*, 4732−4739.
(30) Kruk, M.; Jaroniec, M. Accurate Method for Calculating Mesopore Size Distributions from Argon Adsorption Data at 87 K Developed Using Model MCM-41 Materials. *Chem. Mater.* **2000**, *12*, 222−230.
(31) Jaroniec, M.; Kruk, M.; Olivier, J. Standard nitrogen adsorption data for chracterization of nanoporous silicas. *Langmuir* **1999**, *15*, 5410−5413.
(32) Ustinov, E.; Do, D.; Jaroniec, M. Equilibrium adsorption in cylindrical mesopores: a modified Broekhoff and de Boer theory versus density functional theory. *J. Phys. Chem. B* **2005**, *109*, 1947−1958.
(33) Ustinov, E.; Do, D.; Jaroniec, M. Features of nitrogen adsorption on nonporous carbon and silica surfaces in the frameworks of classical density functional theory. *Langmuir* **2006**, *22*, 6238−6244.
(34) Ravikovitch, P.; Neimark, A. Density functional theory model of adsorption on amorphous and microporous silica materials. *Langmuir* **2006**, *22*, 11171−11179.
(35) Trens, P.; Denoyel, R.; Glez, J. Comparative adsorption of argon and nitrogen for the characterisation of hydrophobized surfaces. *Colloids Surf., A* **2004**, *245*, 93−98.
(36) Kruk, M.; Jaroniec, M. Argon adsorption at 77 K as a useful tool for the elucidation of pore connectivity in ordered materials with large cagelike mesopores. *Chem. Mater.* **2003**, *15*, 2942−2949.
(37) Cychosz, K. A.; Guillet-Nicolas, R.; Garcia-Martinez, J.; Thommes, M. Recent advances in the textural characterization of heirarchically structured nanporous materials. *Chem. Soc. Rev.* **2017**, *46*, 389−414.
(38) Datar, A.; Yoon, S.; Lin, L.-C.; Chung, Y. Brunauer-Emmett-Teller Areas from Nitrogen and Argon Isotherms Are Similar. *Langmuir* **2022**, *38*, 11631−11640.
(39) Kurganov, A.; Trudinger, U.; Isaeva, T.; Unger, K. Native and modified alumina, titania and zirconia in normal and reversed-phase high-performance liquid chromatography. *Chromatographia* **1996**, *42*, 217−222.
(40) Choma, J.; Kloske, M.; Jaroniec, M. An improved methodology for adsorption characterization of unmodified and modified silica gels. *J. Colloid Interface Sci.* **2003**, *266*, 168−174.
(41) Kruk, M.; Jaroniec, M.; Sayari, A. Application of large pore MCM-41 molecular sieves to improve pore size analysis using nitrogen adsorption measurements. *Langmuir* **1997**, *13*, 6267−6273.
(42) Miron, D.; Kendell, S.; Munshi, A.; Alanazi, A.; Brown, T. Time-varying flexible least squares for thermal desorption of gases. *Int. J. Chem. Kinet.* **2013**, *45*, 374−386.
(43) Aslyamov, T.; Khlyupin, A.; Pletneva, V.; Akhatov, I. Theoretical approach to rough surface characterization for silica materials. *J. Phys. Chem. C* **2019**, *123*, 28707−28714.

https://doi.org/10.1021/acs.langmuir.2c02932
Langmuir 2023, 39, 1914−1926

(44) Villiéras, F.; Mamleev, V. S.; Nicholson, D.; Cases, J.-M. Adsorption of spherical molecules in probing the surface topography: 2. Model of conditional probabilities. *Langmuir* **2002**, *18*, 3963−3979.

https://doi.org/10.1021/acs.langmuir.2c02932
Langmuir 2023, 39, 1914−1926